Chemical Engineering Journal 425 (2021) 129051

Contents lists available at ScienceDirect

Chemical Engineering Journal

journal homepage: www.elsevier.com/locate/cej

One-dimensional porous nanostructure composed of few-layered $MoSe_2$ nanosheets and highly densified-entangled-N-doped CNTs as anodes for Na ion batteries

Young Hoe Seon [a], Yun Chan Kang [b], Jung Sang Cho [a,*]

[a] Department of Engineering Chemistry, Chungbuk National University, Gaesin-Dong, Seowon-Gu, Cheongju 361-763, Republic of Korea
[b] Department of Materials Science and Engineering, Korea University, 145, Anam-Ro, Seongbuk-Gu, Seoul 02841, Republic of Korea

ARTICLE INFO

Keywords:
molybdenum diselenide
carbon nanotube composite
sodium ion batteries
anodes
nanofibers
electrospinning

ABSTRACT

Porous nanofibers composed of few-layered $MoSe_2$ nanosheets and highly densified-entangled N-doped carbon nanotubes (N-CNTs) are designed as anodes for Na ion batteries. To maximize the electrical conductivity of the composite nanofibers, amorphous carbon formed by polyacrylonitrile (PAN) decomposition is selectively removed except N-CNTs by intermediate heat treatment. During this step, numerous mesopores are formed between the N-CNTs. Final selenization results in the formation of porous nanofibers composed of few-layered $MoSe_2$ nanosheets and highly densified-entangled-N-CNTs (P-$MoSe_2$/N-CNT NF). The discharge capacity of P-$MoSe_2$/N-CNT NF after 300 cycles is 372 mA h g^{-1}, which is a 100% capacity retention calculated from the 2nd cycle onward. P-$MoSe_2$/N-CNT NF show capacities of 404, 318, 245, 210, 169, 144, 115, and 74 mA h g^{-1} at current densities of 0.2, 2, 5, 7, 10, 12, 15, and 20 A g^{-1}, respectively. Synergetic effects of the N-CNT matrix, uniformly dispersed mesopores, and few-layered $MoSe_2$ nanosheets result in efficient diffusion of Na^+ during uptake/removal and rapid transport of electrons by improving the electrical contact between the $MoSe_2$ nanosheets and electrodes.

1. Introduction

In recent years, transition-metal selenides have received considerable attention as promising anode materials for Na^+ batteries (NIBs) [1–3]. Metal selenides such as $NiSe_2$, $SnSe_2$, $CoSe_2$, $FeSe_2$, and $MoSe_2$ have exhibited superior electrochemical properties compared to their oxides and sulfides when applied as anodes for NIBs [4–8]. The higher capacities of metal selenides as anodes relative to those of the corresponding oxides and sulfides are attributed to reduced energy consumptions during the charge and discharge processes. This is due to the lower formation enthalpy of Na_2Se (−342 kJ mol^{-1}) compared with those of Na_2O (−418 kJ mol^{-1}) and Na_2S (−366 kJ mol^{-1}), weaker binding energy of the metal–Se bond due to the decreased electronegativity of Se, and lower polarizations than their oxide and sulfide counterparts [9,10].

As a representative layered metal selenide, $MoSe_2$ consisting of covalently bonded Se–Mo–Se sandwiched layers has been extensively investigated in many devices, including dye-sensitized cells, electrochemical catalysts, lithium ion batteries (LIBs), and NIBs [8,11,12]. When applied as an anode material for NIBs, $MoSe_2$ possesses a relatively large interlayer spacing of 0.65 nm compared to those of graphite (0.335 nm) and MoS_2 (0.615 nm), enabling the efficient and reversible sodiation/desodiation of Na^+ between layers during repeated cycles [12,13]. However, similar to other metal selenides, $MoSe_2$ also suffers from rapid capacity reduction and large cell resistance when applied as an anode in NIBs due to the drastic volume changes it exhibits during sodiation/desodiation reactions and its low electrical conductivity [4,14,15]. Additionally, $MoSe_2$ nanosheets tend to agglomerate, especially during the heat-treatment process used to prepare anode materials, because of their high surface energy. All of these factors hinder the practical application of $MoSe_2$ as an anode material for high-performance NIBs [16].

Well-designed anode materials have been proven to efficiently enhance the reversible capacities, cycling stabilites, and rate capabilities of NIBs [17,18]. In this regard, the structural design of anode materials can improve NIB performance by shortening the Na^+ and electron pathways, providing a large contact area with the electrolyte, and accommodating the large strain induced by Na^+ diffusion during cycles

* Corresponding authors.
E-mail address: jscho@cbnu.ac.kr (J.S. Cho).

https://doi.org/10.1016/j.cej.2021.129051
Received 26 November 2020; Received in revised form 15 January 2021; Accepted 15 February 2021
Available online 20 February 2021

[19,20]. In addition, carbon nanotubes (CNTs), owing to their high electrical conductivities (107 S m^{-1}) and high aspect ratios, could enable the establishment of an electrical percolation network by incorporating CNTs as a composite material with $MoSe_2$ nanosheets. Specifically, incorporating CNTs could ensure good penetration of the liquid electrolyte into the structure during cycles, which would promote the electrochemical reaction of transition-metal selenide materials when applied as anodes for NIBs. Therefore, various CNT composite structures such as interconnected CNT hybrid nanofibers decorated with Fe_2O_3 [21], three-dimensional interconnected network GeO_x/CNT composite spheres [22], CNT@TiO_2–C composites with 3D networks [23], and mesoporous TiO_2 spheres interconnected by CNTs [24] have been introduced for use in energy storage devices. However, composites of few-layered $MoSe_2$ nanosheets with highly densified and entangled N-CNTs have been difficult to prepare because van der Waals forces between CNTs tend to lead to their aggregation. Moreover, preparation of one-dimensional (1-D) $MoSe_2$/CNT composite nanostructures with numerous pores is quite challenging and has not been reported thus far.

In this study, N-CNTs were highly densified and entangled in a nanofiber structure containing few-layered $MoSe_2$ nanosheets for use as anodes in NIBs by performing acid-treatment of both polyacrylonitrile (PAN) and CNT before electrospinning process. A $MoO_2(acac)_2$–CNT–PAN complex was formed due to dipole–dipole interactions and hydrogen bonding between the CNTs and PAN, which allowed for the formation of a stable jet during the spinning process. As a result, one-dimensional porous nanostructures composed of few-layered $MoSe_2$ nanosheets and highly densified N-CNTs were successfully obtained. In addition, to maximize the electrical conductivity of the composite, the amorphous carbon (AC) formed by PAN carbonization was selectively removed and N was doped into CNTs by an intermediate heat treatment at an optimal temperature. During this step, numerous mesopores were formed between the CNTs and the host materials. After a simple selenization step, highly densified and entangled N-CNT hybrid porous nanofibers decorated with few-layered $MoSe_2$ nanosheets were obtained. The detailed formation mechanism of the porous $MoSe_2$/N-CNTs composite nanofibers and their Na^+ storage performances as anodes in NIBs were investigated in detail.

2. Experimental section

Sample Preparation: Porous nanofibers composed of few-layered $MoSe_2$ nanosheets and highly densified and entangled N-CNTs were prepared via electrospinning and a subsequent two-step heat treatment. The spinning solution was prepared by adding 3.0 g of molybdenyl acetylacetonate ($Mo_2(acac)_2$; $C_{10}H_{16}MoO_6$, ACROS Organics, 97%) and 2.0 g of polyacrylonitrile (PAN, $(C_3H_3N)_n$, Sigma–Aldrich, M_W: 150,000) to a solution obtained by mixing 1.0 g of acid-treated CNTs in 15 mL of dimethylformamide (DMF, Samchun, 99.8%). The acid-treated CNTs (MWCNTs, Cheap Tubes Inc., Cambridgeport, USA; OD: 20–30 nm, length: 10–30 mm, purity: >95.0 wt%) had been prepared by treatment of CNTs in HNO_3/H_2SO_4 (1:3 v/v) acid solution at 80 °C and subsequent freeze-drying. By adding PAN to the DMF solution containing acid-treated CNTs, PAN was also sulfonated by reaction with HNO_3/H_2SO_4 attached to the CNTs dissolved in DMF acid solution. The prepared colloidal solution was loaded into a plastic syringe equipped with a 21-gauge stainless steel nozzle. The loaded solution was ejected at a flow rate of 1.0 mL h^{-1}. The rotation speed of the drum collector was set at 150 rpm. The distance between the tip and collector was fixed at 15 cm. The voltage applied between the collector and syringe tip was maintained at 20 kV. As-spun $MoO_2(acac)_2$/CNT/PAN composite fibers obtained after electrospinning were stabilized at 150 °C for 24 h in air. The stabilized fibers were then treated at 320 °C for 5 h at a heating rate of 5 °C min^{-1} in an air. Finally, selenization was conducted at 550 °C for 5 h under H_2Se gas. During selenization, H_2Se gas was formed by the reaction of H_2 with Se metal powder. As a result, porous nanofibers composed of few-layered $MoSe_2$ nanosheets and highly densified and entangled N-CNTs (denoted as P-$MoSe_2$/N-CNT NF) were obtained. bare-$MoSe_2$ powders were also prepared for comparison. First, bare-MoO_3 powders without carbon were obtained by heat-treatment of as-spun $MoO_2(acac)_2$/CNT/PAN composite nanofibers at 450 °C for 5 h under an air atmosphere. Subsequently, pure $MoSe_2$ powders were obtained after selenization of bare-MoO_3 powders at 550 °C for 10 h.

Characterization Techniques: The microstructures of the samples were observed by field-emission scanning electron microscopy (FE-SEM, Ultra Plus, Zeiss) and field-emission transmission electron microscopy (FE-TEM, JEOL, JEM-2100F). Phase analyses were performed by X-ray diffractometry (XRD, D8 Discover with GADDS, Bruker) using Cu Kα radiation (λ = 1.5418 Å). X-ray photoelectron spectroscopy (XPS, Thermo Scientific, K-Alpha) with focused monochromatic Al Kα radiation at 12 kV and 20 mA was used to analyze the compositions of the samples. The surface areas of the samples were measured by the Brunauer–Emmett–Teller (BET) method using N_2 as the adsorbate gas. Thermogravimetric analysis (TGA) was carried out using a thermogravimetric analyzer (Pyris 1 TGA, Perkin–Elmer) in the temperature range of 25–700 °C at a heating rate of 10 °C min^{-1} in air. The functional groups of the samples were also evaluated using Fourier transform infrared (FT-IR, JASCO, 480 Plus spectrophotometer) spectroscopy. The nitrogen and carbon contents of the samples were analyzed using an elemental analyzer (EA, vario MICRO cube). The characteristics of the carbonaceous materials in the sample were analyzed by Raman spectroscopy (LabRam, HR800, Horiba Jobin-Yvon, Paris, France, excitation source = 515 nm diode laser) at room temperature.

Electrochemical Measurements: The electrochemical properties of the samples were measured by constructing 2032-type coin cells. The working electrode was prepared by mixing the active material, carbon black (Super-P), and sodium carboxymethyl cellulose (CMC) as a binder in a 7:2:1 weight ratio. The electrodes were formed by coating the resulting slurry onto copper foils, which were subsequently dried at 70 °C for 3 h. Na metal and porous polypropylene film were used as the counter electrode and separator, respectively. The carbonate-based electrolyte was prepared by dissolving 1 M $NaClO_4$ and 5% fluoroethylene carbonate (FEC) in a mixture of 1:1 v/v ethylene carbonate (EC) and dimethyl carbonate (DMC). The coin cell was assembled at room temperature in an Ar-filled glove box, where water and oxygen concentrations were kept at less than 1 ppm. The discharge–charge characteristics of the samples were measured at various current densities in the voltage range of 0.001–3.0 V. Cyclic voltammetry measurements were performed at a scan rate of 0.01 mV s^{-1}. The working electrode containing the samples was 1.4 × 1.4 cm^2, and the mass loading was approximately 1.2 mg cm^{-2}. The capacities of the samples were calculated based on the total mass of the prepared sample. Electrochemical impedance spectra were obtained by performing alternating-current electrochemical impedance spectroscopy (EIS, ZIVE SP1) over a frequency range of 0.01 Hz to 100 kHz with a signal amplitude of 10 mV.

3. Results and discussion

A 1-D porous nanostructure composed of few-layered $MoSe_2$ nanosheets and highly densified and entangled N-CNTs (denoted as P-$MoSe_2$/N-CNT NF) was prepared via electrospinning and a subsequent two-step heat treatment. Precursor $MoO_2(acac)_2$/CNT/PAN composite fibers were first prepared by electrospinning, as shown in Fig. 1. The uniform thickness of the fibers formed after spinning was 700 nm, which indicates that the CNTs were not partially aggregated in the fiber structure during spinning, as shown in Fig. 1a. The composite fibers have slightly wrinkled surfaces in Fig. 1b due to the outward diffusion of PAN. As seen in the image of the fractured surface of a fiber shown in Fig. 1b, highly densified and entangled CNTs are clearly observed. In general, van der Waals forces between CNTs in colloidal spinning solutions tend to induce aggregation of CNTs, which then form nonuniform fiber products with bimodal thicknesses after spinning. However, in this study, acid treatment of both CNT and PAN effectively prevented the aggregation of

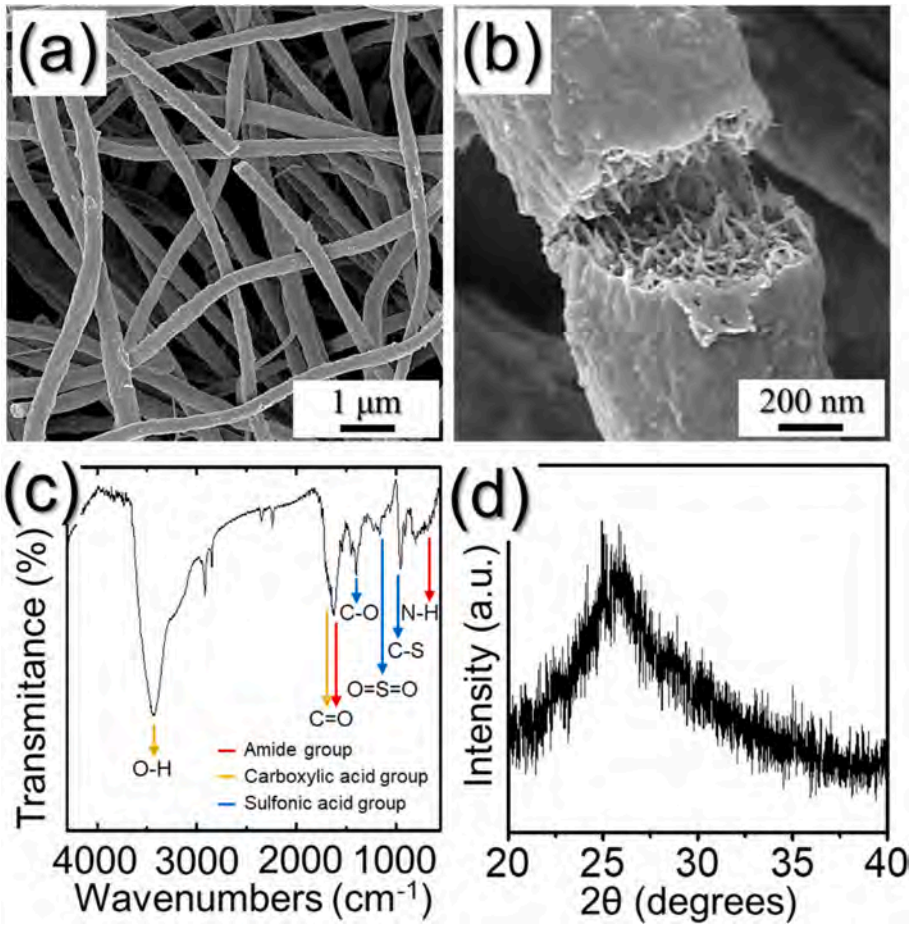

Fig. 1. As-spun $MoO_2(acac)_2$/CNT/PAN composite nanofibers obtained after electrospinning: (a,b) FE-SEM images, (c) FT-IR spectrum, and (d) XRD pattern.

CNTs, forming homogeneous complexes of $MoO_2(acac)_2$–CNT–PAN in DMF solvent. It is expected that CNTs with carboxylic acid groups (–COOH) have dipole–dipole and hydrogen bonding interactions with sulfonated polyacrylamide groups of modified PAN. By adding PAN to the DMF solution with acid-treated CNTs, PAN was also sulfonated by reaction with HNO_3/H_2SO_4 attached to the CNTs dissolved in DMF acid solution. Therefore, the electrophilic nitrile (–C≡N) group of PAN is hydrolyzed to form a sulfonated polyacrylamide ($–SO_3H$, O=C–NH_2) group. As seen in Fig. 1c, the presence of relevant functional groups (N–H at 588 cm^{-1}, C–S at 1040 cm^{-1}, O=S=O at 1197 cm^{-1}, C–N at 1214 cm^{-1}, and C=O at 1580 cm^{-1}) was verified by FT-IR [21,25,26]. The presence of carboxylic acid groups (–COOH) on the CNTs was also confirmed by FT-IR (C=O at 1640 cm^{-1} and O-H at 3400 cm^{-1}) [27,28]. Additional FT-IR spectra of PAN and CNT before and after acid treatments are shown in Fig. S1. From the XRD result in Fig. 1d, a broad pattern attributed to CNTs at 25° was confirmed and additional peaks were not observed, which confirms the amorphous-like $MoO_2(acac)_2$ phase of the as-spun fibers before heat treatment.

In this study, a heat-treatment process was carried out to generate pores in the structure between CNTs and active materials by selectively removing AC formed by PAN decomposition as gas products while remaining CNTs. The resulting porous structure can ensure good electrolyte penetration, easy accommodation of the volume variations of anodes during repeated cycles, and preservation of the structural integrities of the anodes during cycles. Additionally, AC, whose electrical conductivity is lower than that of CNTs, could be eliminated selectively during the intermediate heat-treatment process. Therefore, it is expected that the composite nanofibers will facilitate rapid electron transfer by improving the electrical contact between the active sites and the electrode when the sample is used as an NIB anode. In order to select the optimal heat-treatment temperature to selectively remove AC and inhibit grain growth of MoO_3 crystals, the morphologies of the samples are examined at various temperatures from 250 to 400 °C, as depicted in Fig. 2. During heat treatment, the decomposition of $MoO_2(acac)_2$, CNT, and PAN in the as-spun fibers occur sequentially. As the temperature increases from 250 to 320 °C, $MoO_2(acac)_2$ decomposes and is converted to MoO_3 crystals from the XRD results (Fig. 2f-h). Subsequently, decomposition of AC occurs, so that the AC covering on the fiber surface and located between CNTs is selectively removed, exposing the inner CNTs, as shown in Fig. 2c. Interestingly, it should be noted that even at 320 °C, large grain growth of MoO_3 is not observed, because the carbon surrounding the MoO_3 nanosheets prevented grain growth. However, rapid grain growth of the MoO_3 nanosheets occurs above 320 °C, generating MoO_3 sheets over 400 nm attached to or separated from the fibrous structure (Fig. 2d). Finally, at 400 °C, complete thermal decomposition of CNTs occurs, which results in bulky pure MoO_3 plates without any other contents (Fig. 2e). As the temperature increased from 320 to 400 °C, the crystallite size of MoO_3 also increased as shown in Fig. 2h-j. The changes in the color of the samples with increasing temperature, from black to white, indicate the complete decomposition of carbon or CNTs into gas in the remaining MoO_3 plates. Concurrently, the initial sheet-type structure, as shown in Fig. 2a, is gradually broken into pieces with increasing temperature, finally forming a powder, as shown in Fig. 2e. From the results, the optimal heat-treatment temperature to selectively remove AC and inhibit the grain growth of MoO_3 crystals of the composite was determined to be 320 °C.

The detailed morphologies of the nanofibers composed of MoO_3 nanoparticles and highly densified CNTs obtained after heat treatment at the optimal temperature of 320 °C are shown in Fig. 3. During the treatment, PAN coating the fiber surfaces located between the CNTs and

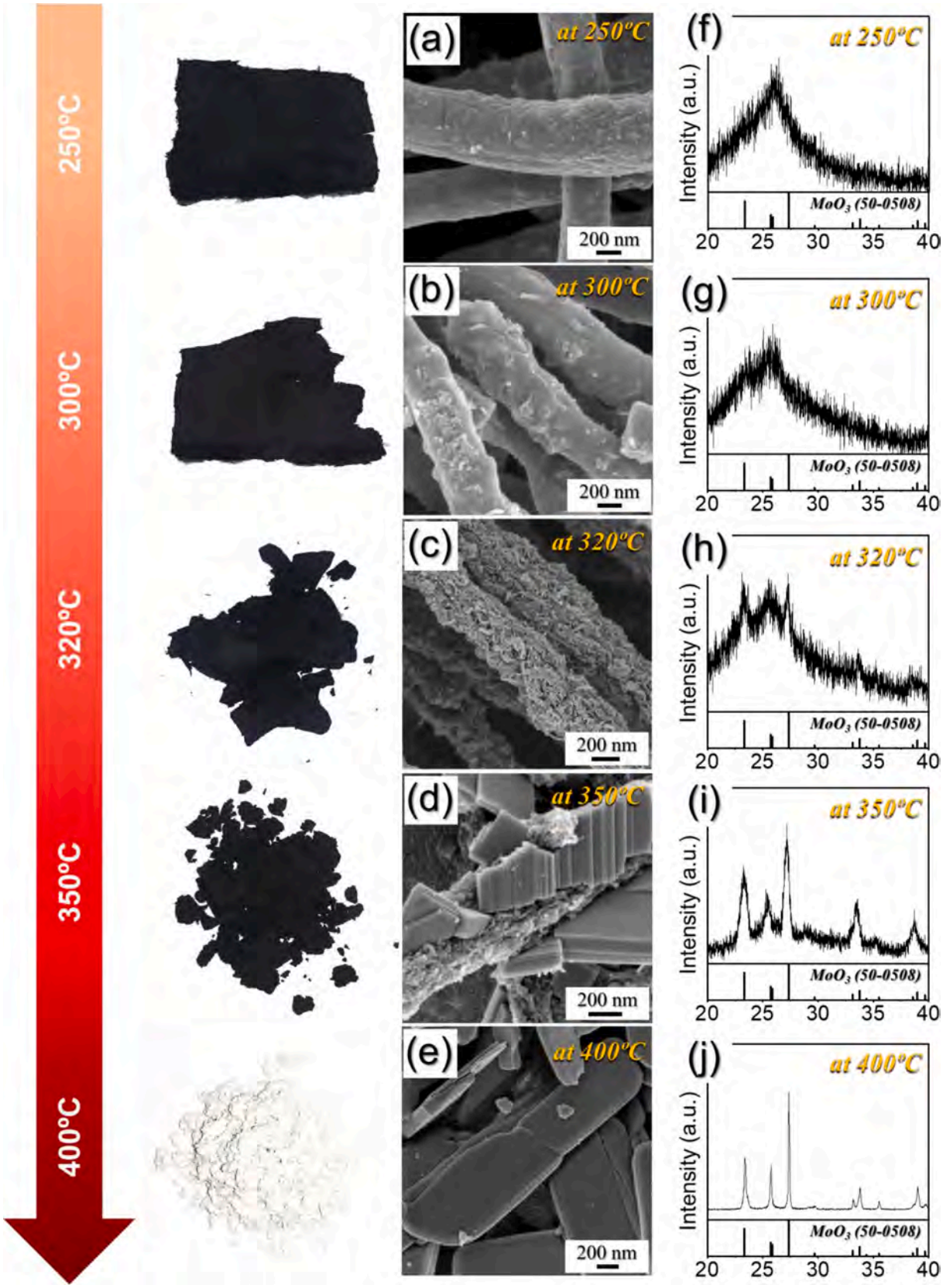

Fig. 2. Morphologies, digital images, and XRD patterns of the nanofibers obtained after heat-treatments of as-spun nanofibers under air atmosphere at various temperatures: (a,f) 250 °C, (b,g) 300 °C, (c,h) 320 °C, (d,i) 350 °C, and (e,j) 400 °C.

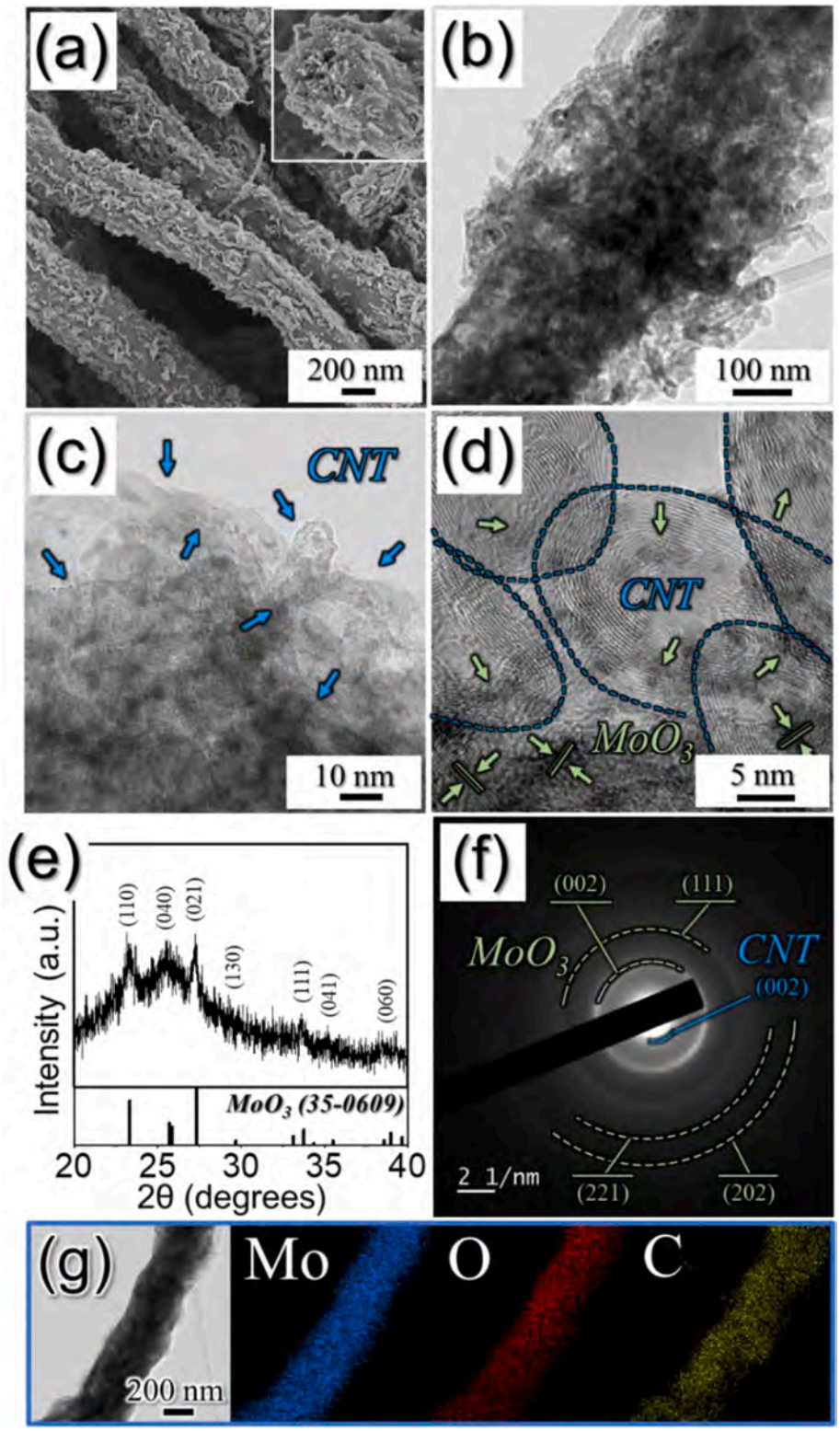

Fig. 3. Porous MoO_3/CNT composite nanofibers obtained after heat-tretment of as-spun nanofibers at 320 °C for 5 h under air atmosphere: (a) FE-SEM image, (b) TEM image, (c,d) HR-TEM images, (e) XRD pattern, (f) SAED pattern, and (g) elemental mapping images.

MoO_3 nanoparticles decomposed into AC and was then selectively removed as gas, resulting in a porous structure, as shown in Fig. 3a–c. We confirmed that the PAN starts to degrade quickly, generating many gaseous compounds (e.g., HCN, CO, and CO_2) from the cyclization reaction and completed the decomposition at around 370 °C, as shown in the TGA data (Fig. S2a). On the other hand, CNTs are not decomposed until the heat treatment temperature reached approximately 360 °C (Fig. S2b). As a result, inner CNTs covered with PAN are exposed to the nanofiber surface, as shown in Fig. 3a and b. The average thickness of the nanofibers shrunk from 700 to 400 nm after heat treatment. The porous nanostructure linked with highly entangled CNTs is clearly observed by TEM (Fig. 3b–d). Additionally, $MoO_2(acac)_2$ of the as-spun

fibers is converted into MoO_3 crystals of nanoscale dimensions, which are uniformly distributed throughout the structure along with CNTs, as indicated by the arrows in Fig. 3d. The XRD and selected area electron diffraction (SAED) patterns in Fig. 3e and f further confirm the formation MoO_3 nanoparticles with of low crystallinity. Using Scherrer's equation and the width of the (021) peak of MoO_3, the mean crystallite size of the orthorhombic MoO_3 in the structure was calculated to be 2.2 nm. This indicated that the grain growth of the MoO_3 nanocrystals was efficiently inhibited at the optimal temperature of 320 °C by being surrounded by the carbon that originated from PAN during heat

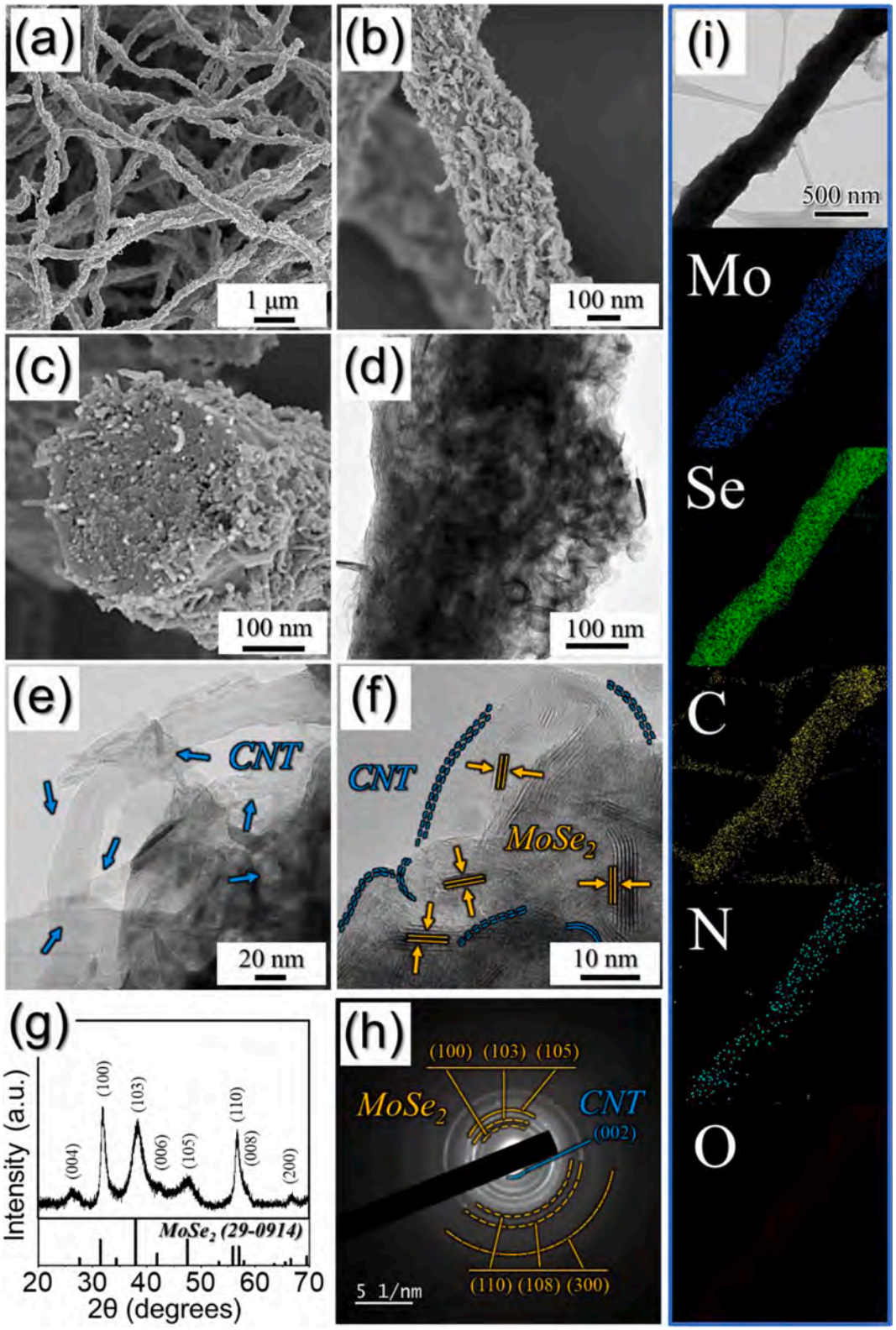

Fig. 4. P-$MoSe_2$/N-CNT NF obtained after selenization of porous MoO_3/CNT composite nanofibers at 550 °C for 5 h: (a-c) FE-SEM images, (d) TEM image, (e,f) HR-TEM images, (g) XRD pattern, (h) SAED pattern, and (i) elemental mapping images.

treatment. The elemental dot mapping images in Fig. 3g show the formation of MoO_3 nanocrystals, which are homogeneously distributed throughout the CNT-matrixed nanofiber structure.

Finally, porous nanofibers composed of few-layered $MoSe_2$ nanosheets and highly densified and entangled N-CNTs are obtained after selenization, as shown in Fig. 4. Even after heat treatment of the sample at 550 °C for 5 h, the overall CNT-matrixed fibrous nanostructure is maintained well, as shown in Fig. 4a and b. As seen in the fractured surface FE-SEM (Fig. 4c) and TEM (Fig. 4d and e) images of the nanofibers, the highly densified and interconnected CNTs are preserved. The continuous framework of CNTs and the interconnected morphology of 1-D structured CNTs are expected to provide favorable pathways to facilitate charge transfer during cycling. Additionally, MoO_3 particles of nanoscale dimensions between CNTs are completely converted into few-layered $MoSe_2$ nanosheets, as seen in the HR-TEM image in Fig. 4f. MoO_3 crystals reacted with hydrogen selenide (H_2Se) gas during selenization, resulting in the formation of few-layered $MoSe_2$. To reliably verify whether MoO_3 converted into $MoSe_2$ completely after selenization, quantitative analyses (EDS and EA) of P-$MoSe_2$/N-CNT NF were carried out (Fig. S3). Any peak and content corresponding to oxygen content were not detected at all in both EDS and EA results. Therefore, it was verified that the phase conversion of MoO_3 into $MoSe_2$ occurred completely at 550 °C for 5 h. As with the MoO_3 nanocrystals that were generated during the first heat treatment, the grain growth of $MoSe_2$ and stacking of these nanosheets during selenization could also be inhibited efficiently by being surrounded by CNTs. The $MoSe_2$ with a few-layered nanosheet structure is expected to have improved conductivities of both Na^+ and electrons compared to those of larger and thicker stacked $MoSe_2$ sheets due to increased contact area between the electrolyte and $MoSe_2$ nanosheets during the charge/discharge process. In addition, the

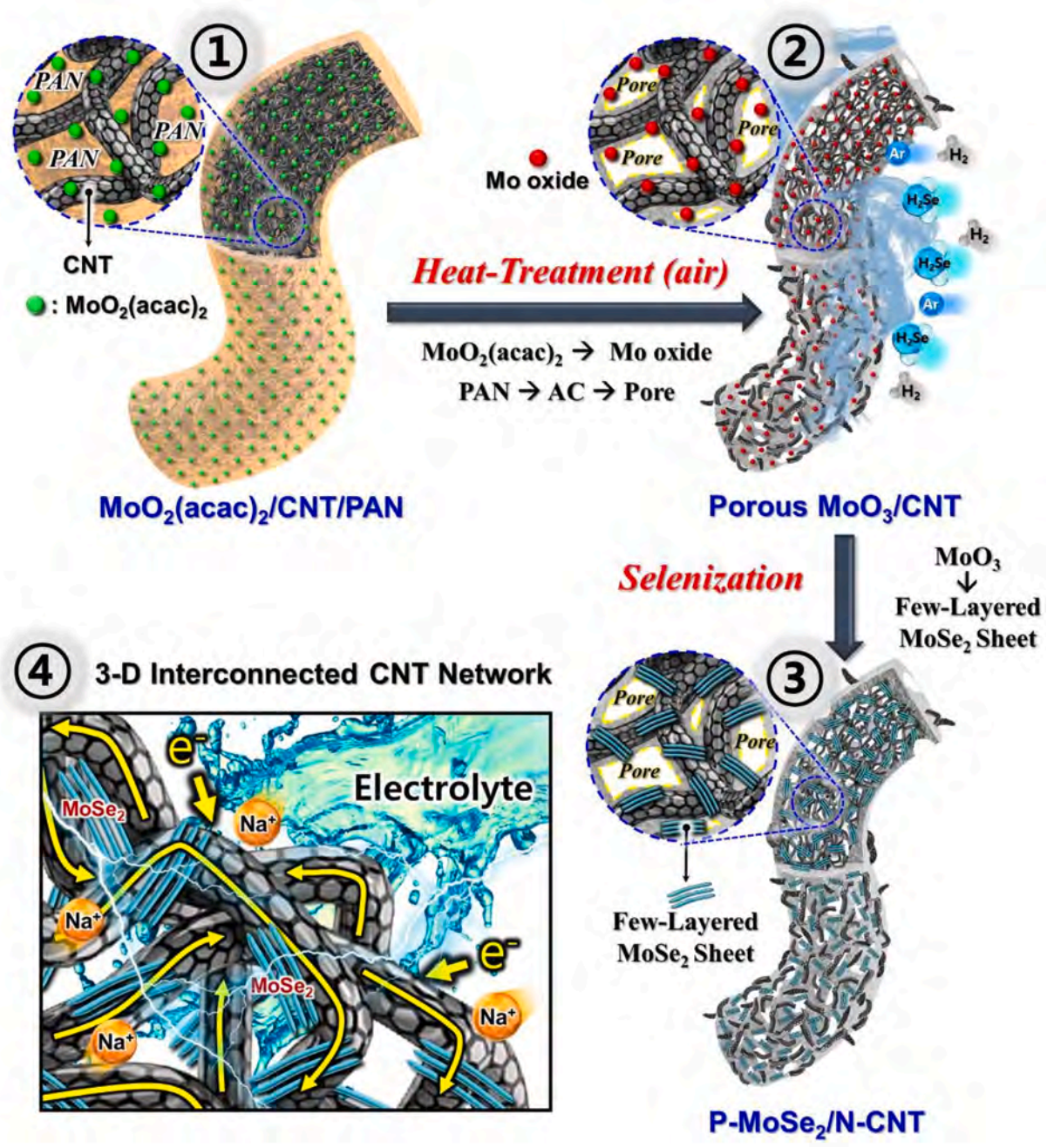

Scheme 1. Formation mechanism of P-$MoSe_2$/N-CNT NF by electrospinning and subsequent heat-treatments.

PAN that was originally present acted as an N-doping source during the first heat treatment, and N was eventually doped into the CNT structure to form N-CNTs even after selenization. N-CNTs are promising as anodes for improving the electrical conductivity of the cell. In Fig. 4g, the XRD pattern further indicated the successful conversion of MoO_3 nanoparticles into $MoSe_2$. The mean crystallite size of $MoSe_2$ calculated using Scherrer's equation and the width of the (103) peak was 3.94 nm. The SAED pattern (Fig. 4h) also confirmed formation of a composite of a hexagonal $MoSe_2$ phase and CNTs. The elemental dot mapping images of P-$MoSe_2$/N-CNT NF (Fig. 4i) clearly show the uniform distribution of molybdenum, selenium, carbon, and nitrogen over the entire composite structure. In other words, few-layered $MoSe_2$ nanosheets have uniform

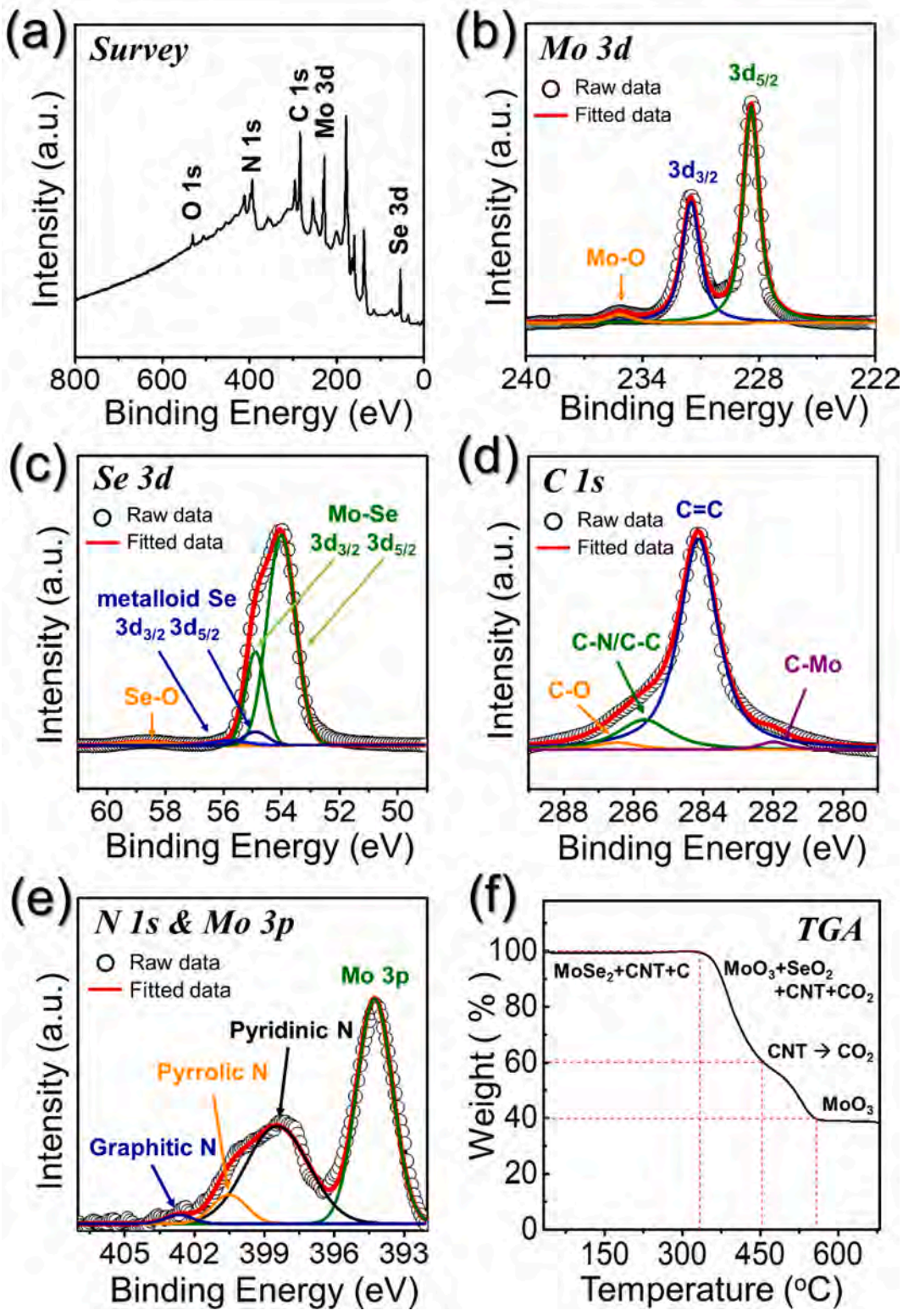

Fig. 5. XPS spectra and TGA curve of P-$MoSe_2$/N-CNT NF obtained after selenization: (a) XPS survey spectrum, (b) Mo 3d XPS spectrum, (c) Se 3d XPS spectrum, (d) C 1s XPS spectrum, (e) N 1s and Mo 3p XPS spectra, and (f) TGA curve.

composition throughout the entire porous N-CNT networks.

A schematic of the detailed formation mechanism of P-$MoSe_2$/N-CNT NF is summarized in Scheme 1. The precursor as-spun $MoO_2(acac)_2$/CNT/PAN composite fibers are prepared by a spinning process (Scheme 1-①). During spinning, aggregation of CNTs induced by van der Waals forces can be effectively prevented by acid treatments of both CNT and PAN, forming homogeneous complexes of $MoO_2(acac)_2$–CNT–PAN in the structure. During oxidation (Scheme 1-②), $MoO_2(acac)_2$ in the as-spun fibers is converted into MoO_3 crystals of nanoscale dimensions, which are uniformly distributed throughout the structure. The grain growth of MoO_3 can be inhibited by being surrounded by carbon originating from PAN. Additionally, PAN is decomposed into AC and subsequently removed selectively as gas, which generates pores between the CNTs. The porous nanofibers composed of few-layered $MoSe_2$ nanosheets and highly densified N-CNTs are finally obtained after selenization (Scheme 1-③). MoO_3 crystals between N-CNTs are completely converted into $MoSe_2$ nanosheets. The grain growth of $MoSe_2$ and the stacking of these during selenization can also be inhibited efficiently by being surrounded by N-CNTs. Scheme 1-④ shows the efficient transfer mechanisms of Na^+ and electrons through few-layered $MoSe_2$ nanosheets and N-CNT matrix during the charge/discharge process.

To elucidate the chemical nature of the P-$MoSe_2$/N-CNT NF, XPS analysis was performed; results are shown in Fig. 5. The signals corresponding to Mo, Se, C, and N in the structure are shown in the XPS survey scan (Fig. 5a). In the Mo 3d spectrum (Fig. 5b), the Mo $3d_{3/2}$ and Mo $3d_{5/2}$ binding energies of $MoSe_2$ are confirmed from the peaks at 231.7 and 228.4 eV, respectively [29,30]. The additional XPS peak at 235.2 eV for the Mo $3d_{5/2}$ state of the MoO_3 phase is due to surface oxidation of $MoSe_2$ that occurs upon exposure to air [31–34]. In the Se 3d spectrum (Fig. 5c), characteristic peaks for $MoSe_2$ are also observed at 54.9 eV (Se $3d_{3/2}$) and 54.1 eV (Se $3d_{5/2}$) [8,35]. Metalloid Se peaks with low intensities are observed at 55.9 eV (Se $3d_{3/2}$) and 55.1 eV (Se $3d_{5/2}$) due to the infiltration of metalloid Se into the structure during selenization [36,37]. Additionally, the Se–O peak at 58.7 eV is attributed to SeO_2 formed from to the exposure of P-$MoSe_2$/N-CNT NF to air [38,39]. The C 1s spectrum (Fig. 5d) contains peaks corresponding to C=C, C–N/C-C, and C-O bonds at 284.2, 285.7, and 286.4 eV, respectively [40,41]. The additional C–Mo bond at a binding energy of 282.3 eV is also confirmed [29]. The N 1s spectrum (Fig. 5e) showed pyridinic-N, pyrrolic-N, and graphitic-N at binding energies of 398.4, 400.5, and 402.6 eV, along with a Mo 3p signal at 394.2 eV [29,42,43]. The TGA curve in Fig. 5f illustrates the thermal behavior of the P-$MoSe_2$/N-CNT NF under air. The initial slight weight increase at 270 °C is due to the partial oxidation of $MoSe_2$ to form MoO_3 and SeO_2 [44,45]. Weight loss was observed in the temperature range of 330–550 °C. The first weight loss between 320 and 450 °C is due to the volatilization of SeO_2 in the air atmosphere. The second weight loss starting at approximately 450 °C is due to the subsequent decomposition of N-CNTs. From the TGA and EA (Fig. S3) analyses, the N-CNT content of P-$MoSe_2$/N-CNT NF was calculated to be approximately 23.08%. Additionally, the N-doping content in P-$MoSe_2$/N-CNT NF is 2.05 wt%, which is promising for improving the electrical conductivities of the anodes. Raman spectroscopy was employed to investigate the carbon structures of the P-$MoSe_2$/N-CNT NF (Fig. S4). It shows peaks at 1346 cm^{-1} (carbon D band) and 1580 cm^{-1} (carbon G band). The peak intensity ratio between the D and G bands (I_D/I_G) is 1.38, indicating the formation of defects in CNTs during heat treatments [6].

In order to prove the synergetic structural effects of P-$MoSe_2$/N-CNT NF on the Na^+ storage properties, bare-$MoSe_2$ powders were also prepared for comparison by a two-step heat treatment. In this process, bare-MoO_3 plates without carbon are first obtained after oxidation of the as-spun $MoO_2(acac)_2$/PAN composite nanofibers at 450 °C in air (Fig. S5). During oxidation, $MoO_2(acac)_2$ and PAN are converted into MoO_3 and CO_2 gas, respectively, by decomposition. As a result, MoO_3 plates with a width of 800 nm are obtained, as shown in Fig. S5a. Subsequently, selenization of the bare-MoO_3 plates at 550 °C finally produces phase-pure $MoSe_2$ powders with well-developed and clear lattice fringes, as shown in Fig. 6. Highly stacked Se–Mo–Se layers are formed during the selenization process, as shown in the HR-TEM image (Fig. 6c). Stacking of $MoSe_2$ layers was not suppressed, as there was no disrupter such as carbon between crystals. Therefore, stacked lattice fringes with a separation of 0.65 nm corresponding to the (002) crystal plane of the hexagonal $MoSe_2$ phase are clearly observed. The XRD (Fig. 6d) and SAED (Fig. 6e) patterns further confirm the formation of phase-pure $MoSe_2$ powders. In addition, the elemental mapping images shown in Fig. 6f also confirm the complete conversion of MoO_3 to $MoSe_2$ without carbon during selenization. N_2 adsorption and desorption isotherms and Barrett–Joyner–Halenda (BJH) pore size distributions of the P-$MoSe_2$/N-CNT NF and the bare-$MoSe_2$ powders are shown in Fig. S6. The hierarchically porous N-CNT matrixed fibrous structure and few-layered $MoSe_2$ nanosheets have higher BET surface area (36.5 $m^2\ g^{-1}$) than the bare-$MoSe_2$ powders (5.1 $m^2\ g^{-1}$). The Barrett–Joyner–Halenda pore size distribution of P-$MoSe_2$/N-CNT NF shown in Fig. S6b indicates the presence of mesopores formed between CNTs owing to the selective removal of AC from the structure.

The Na^+ storage properties of the P-$MoSe_2$/N-CNT NF and the bare-$MoSe_2$ powders as anode materials for NIBs were thoroughly investigated. The cyclic voltammogram (CV) of P-$MoSe_2$/N-CNT NF for the first three cycles at a scan rate of 0.1 mV s^{-1} over the potential range of 0.001–3.0 V (vs Na^+/Na) is shown in Fig. 7a. In the first cathodic scan, the broad shoulder peak at 1.06 V is attributed to the intercalation of Na^+ ions into the interlayer of $MoSe_2$, resulting the formation of the Na_xMoSe_2 [12,46]. The following peaks observed at 0.66 and 0.41 V are attributed to the reaction of Na_xMoSe_2 and Na^+ ions into hexagonal Na_2Se and metallic Mo [12,29]. In the first anodic step, a major peak is observed at 1.82 V accompanied by a shoulder at 2.14 V. The peak at 1.82 V corresponds to the conversion reaction of Na_2Se with metallic Mo into $MoSe_2$ [47,48]. The additional shoulder peak at 2.14V is due to the Na-Se reaction as follows ($Na_2Se \rightarrow Se + 2Na$) [46]. From the second cathodic scan onward, the peaks observed in the first cathodic scan disappear, implying that an irreversible electrochemical reaction occurs. However, two new broad peaks at 1.78 and 1.39 V are observed. The peak at 1.78 V is attributed to the Na–Se reaction as follows ($Se + 2Na \rightarrow Na_2Se$) [49,50]. Moreover, the peak at 1.39 V corresponds to the conversion reaction of $MoSe_2$ with Na^+ to Na_2Se [50,51]. For the second discharge/charge process, the CV curves overlap substantially, suggesting the occurrence of the highly reversible electrochemical reaction processes of P-$MoSe_2$/N-CNT NF. Therefore, the Na^+ reaction mechanism is described as the following equations:

First discharge process:

$MoSe_2 + xNa^+ + xe^- \rightarrow Na_xMoSe_2$ (1)

$Na_xMoSe_2 + (4 - x)Na^+ + (4 - x)e^- \rightarrow 2Na_2Se + Mo$ (2)

Reversible charge/discharge process:

$2Na_2Se + Mo \leftrightarrow MoSe_2 + 4Na^+ + 4e^-$ (3)

$Na_2Se \leftrightarrow Se + 2Na^+ + 2e^-$ (4)

In the case of bare-$MoSe_2$, the reaction mechanism is similar to that of P-$MoSe_2$/N-CNT NF, resulting in a similar CV curve. However, the reduction peaks of bare-$MoSe_2$ are located at slightly lower potentials than those of P-$MoSe_2$/N-CNT NF, which proves that intercalation/deintercalation of Na^+ proceeds more efficiently in the structure of P-$MoSe_2$/N-CNT NF. The few-layered $MoSe_2$ nanosheet structure boosted the conductivities of Na^+ and electrons of the P-$MoSe_2$/N-CNT NF compared to the larger and thicker stacked $MoSe_2$ sheets of bare-$MoSe_2$ by increasing the contact area between the electrolyte and $MoSe_2$ nanosheets during the charge/discharge process.

The initial discharge and charge curves of both samples at a current density of 0.2 A g^{-1} are shown in Fig. 7c. The plateau in P-$MoSe_2$/N-CNT NF corresponding to the discharge/charge process exactly reflects the peak positions obtained from the CV curves. However, the cathodic peaks of the bare-$MoSe_2$ in the first-cycled CV curve do not correspond to its discharge-charge profiles. This is due to the polarization of the

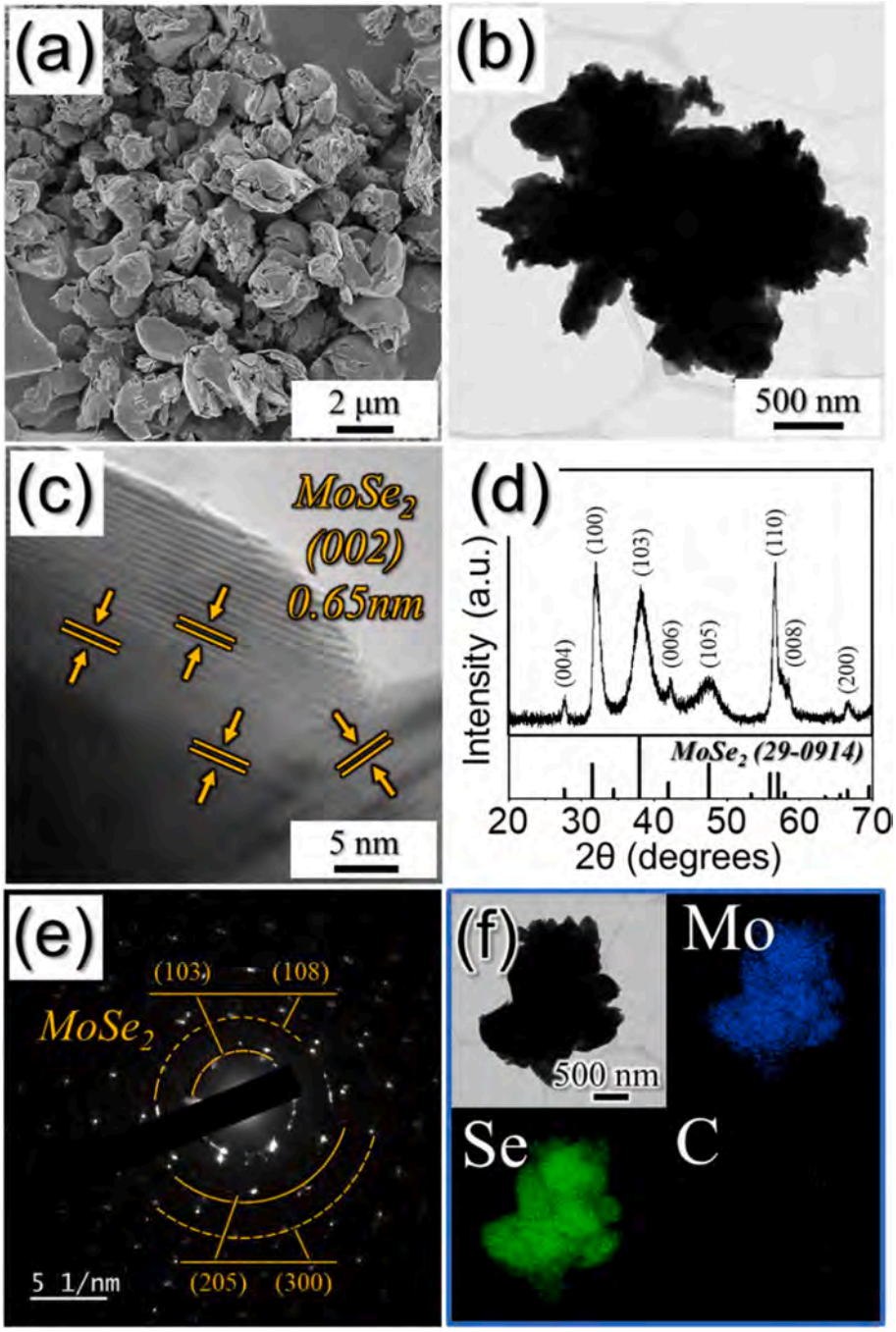

Fig. 6. Morphologies, XRD, SAED patterns, and elemental mapping images of the bare-$MoSe_2$ powders obtained after selenization at 550 °C for 10 h: (a) FE-SEM image, (b) TEM image, (c) HR-TEM image, (d) XRD pattern, (e) SAED pattern, and (f) elemental mapping images.

bare-$MoSe_2$ caused by slow sodium ion diffusion into the structure [6,52]. In this study, the discharge and charge profiles of the bare-$MoSe_2$ were analyzed at a relatively high current density of 0.2 A g^{-1}. Therefore, Na^+ intercalation/deintercalation reactions could not proceed well in the bare-$MoSe_2$ powders with filled structure. To verify this, the initial discharge-charge profiles of the bare-$MoSe_2$ powders were confirmed at a lower current density of 0.01 A g^{-1} (Fig. S7). In the first discharge process, the plateaus corresponding to the cathodic peaks of the bare-$MoSe_2$ powders could be observed, which is match well with its CV result. During discharging, bare-$MoSe_2$ clearly shows a long and distinctive plateau at a lower potential of 0.6 V, whereas the P-$MoSe_2$/N-CNT NF exhibit a steep and unclear plateau at the higher level. Additionally, the samples showed a difference in voltage hysteresis (ΔV = 1.21 V for P-$MoSe_2$/N-CNT NF and 1.47 V for bare-$MoSe_2$), which is due to the polarization caused by slow Na^+ diffusion into bare-$MoSe_2$ and the higher crystallite size of bare-$MoSe_2$ [6,52]. This clearly suggested that the P-$MoSe_2$/N-CNT NF could facilitate better ion and electron conduction, which is highly promising for high-rate NIB anodes. The initial discharge capacities of P-$MoSe_2$/N-CNT NF and bare-$MoSe_2$ are 531 and 472 mA h g^{-1}, respectively, and their corresponding Coulombic efficiency (CE) values are 74 and 84%, respectively. The relatively low CE of P-$MoSe_2$/N-CNT NF was attributed to the presence of N-CNTs with a high initial irreversible capacity loss in the composite [53]. The galvanostatic charge-discharge (GCD) profiles of samples for selected cycles of the 1^{st}, 2^{nd},5^{th}, 10^{th}, 50^{th}, 100^{th}, 150^{th}, 200^{th}, and 300^{th} cycles are also shown in Fig. S8.

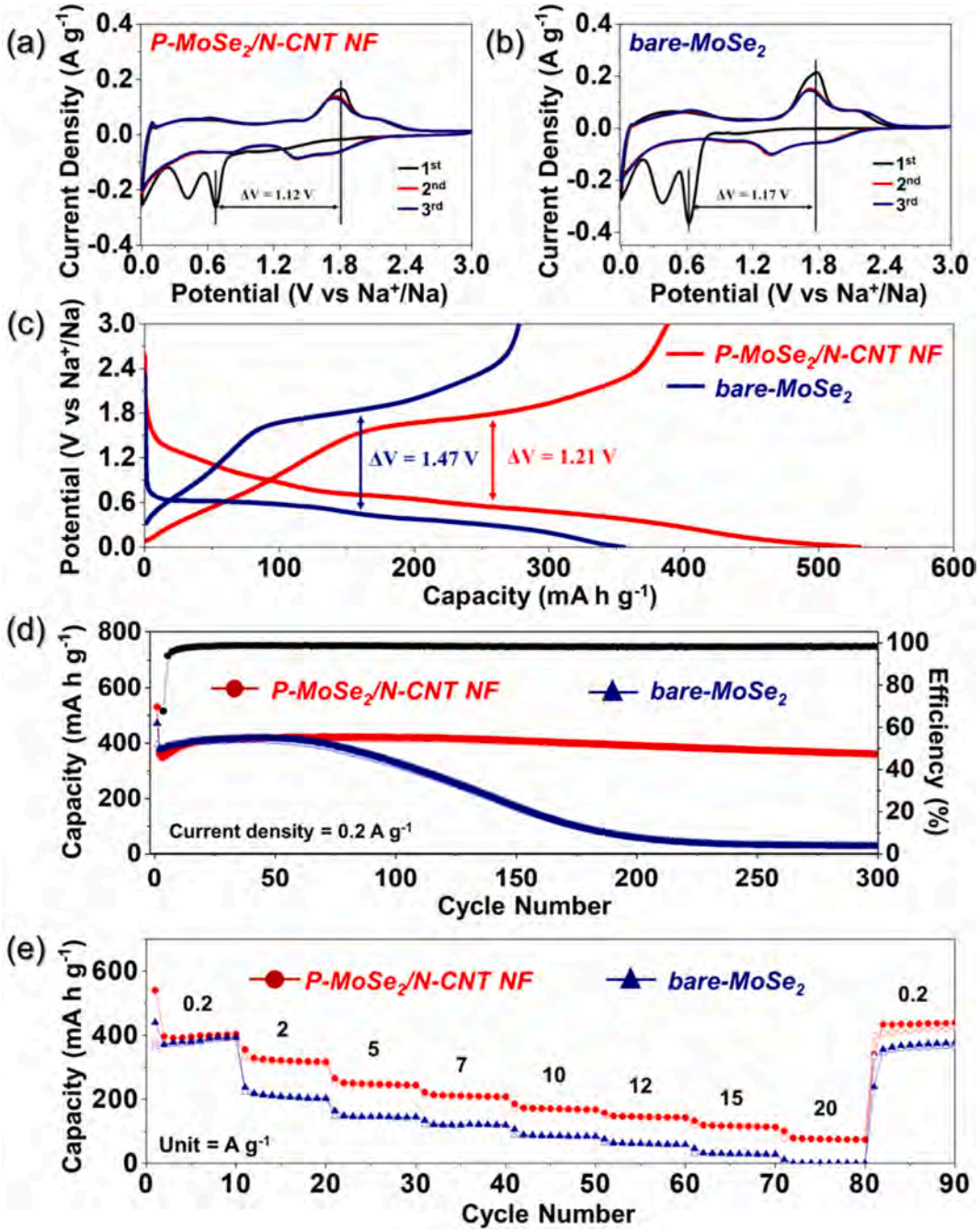

Fig. 7. Electrochemical properties of P-$MoSe_2$/N-CNT NF and bare-$MoSe_2$ powders for sodium-ion storage: (a) CV curve of P-$MoSe_2$/N-CNT NF, (b) CV curve of bare-$MoSe_2$ powders, (c) first discharge/charge curves at the current density of 0.2 A g^{-1}, (d) cycling performances at a current density of 0.2 A g^{-1}, and (e) rate performances.

The cycle properties of the samples at a current density of 0.2 A g^{-1} are shown in Fig. 7d. The bare-$MoSe_2$ powders maintain their capacities up to the initial 50th cycle. However, after the cycles, the capacities continuously decrease to 27 mA h g^{-1} after 300 cycles because the large and thick stacked $MoSe_2$ sheets of the bare-$MoSe_2$ without C could not accommodate the huge strain induced by the volume variations of the active materials during repeated Na^+ insertion–desertion processes. In contrast, the P-$MoSe_2$/N-CNT NF show superior cycle properties over 300 cycles. A capacity increase for P-$MoSe_2$/N-CNT NF is observed during the initial 50 cycles. This phenomenon is well known for most transition-metal oxide anode materials because of formation of a polymeric gel-like film on the active materials during the initial cycling [54–56]. Additionally, the formation of a polymeric gel-like film is promoted by the presence of small grains and particle sizes, as is the case with the P-$MoSe_2$/N-CNT NF described in this study [55,56]. The discharge capacity of the P-$MoSe_2$/N-CNT NF after 300 cycles is 372 mA h g^{-1}, which is a 100% capacity retention calculated from the 2nd cycle onward, and its corresponding CE is 99.2%. The uniformly dispersed few-layered $MoSe_2$ nanosheets, CNTs, and mesopores in the structure provided a degree of buffering against volume variations that accompany Na^+ sodiation/desodiation processes. It therefore efficiently prevented pulverization and agglomeration of $MoSe_2$ nanosheet anode materials, leading to improved structural stability during cycling. In order to prove 1-D structural effect of P-$MoSe_2$/N-CNT NF on the Na^+ storage properties, $MoSe_2$/CNT hybrid was prepared by directly compositing $MoSe_2$ powders and CNTs with the identical content ratio

as P-$MoSe_2$/N-CNT NF in Fig. S9. It showed quite poor cycle property. The initial discharge capacity of the $MoSe_2$/CNT composite is 532 mA h g^{-1}, and its corresponding Coulombic efficiency value is 59%. The discharge capacity of the sample after 300 cycles is 63 mA h g^{-1}, which is a 19% capacity retention calculated from the 2nd cycle onward. Form the result, it is proved that the P-$MoSe_2$/N-CNT NF provides sufficient structure benefits for Na storage performance. The continuous framework of CNTs and the interconnected morphology of 1-D structured CNTs provide favorable pathways to facilitate charge transfer during cycling. The capacity contribution of CNTs to the P-$MoSe_2$/N-CNT NF anode was calculated by etching P-$MoSe_2$/N-CNT NF with HCl solution to obtain pure CNT frameworks. Complete removal of $MoSe_2$ from the structure is confirmed by EDS data, as shown in Fig. S10b. The first discharge–charge profile shows the general curves of carbonaceous materials with discharge and charge capacities of 721 and 266 mA h g^{-1}, respectively (Fig. S10c). The pure CNT framework exhibits a reversible discharge capacity of 222 mA h g^{-1} at a current density of 0.2 A g^{-1} for the 50th cycle, as shown in Fig. S10d. From the result, the CNT framework was estimated to contribute to 52% discharge capacity of the P-$MoSe_2$/N-CNT NF anode.

The rate properties of P-$MoSe_2$/N-CNT NF and bare-$MoSe_2$ when the current density is increased stepwise from 0.2 to 20.0 A g^{-1} are shown in Fig. 7e. The discharge capacity of bare-$MoSe_2$ rapidly decreases from 393 mA h g^{-1} to almost zero when the current density is increased from 0.2 to 20.0 A g^{-1}. On the other hand, the P-$MoSe_2$/N-CNT NF exhibits an excellent rate performance even at high current densities. P-$MoSe_2$/N-CNT NF shows capacities of 404, 318, 245, 210, 169, 144, 115, and 74 mA h g^{-1} at current densities of 0.2, 2, 5, 7, 10, 12, 15, and 20 A g^{-1}, respectively. In addition, the discharge capacity recovers to 440 mA h g^{-1} when the current density returns to 0.2 A g^{-1}, even after operation at extremely high current densities. The excellent rate properties of the P-$MoSe_2$/N-CNT NF are attributed to the synergetic effects of the highly integrated N-CNT matrix with high electrical conductivity, few-layered $MoSe_2$ nanosheets, and numerous pores between the $MoSe_2$/N-CNT composite. The N-CNTs significantly improved the overall electrical conductivity of the $MoSe_2$ composite, and the uniformly dispersed pores enabled efficient penetration of the liquid electrolyte into the structure. Moreover, the few-layered $MoSe_2$ nanosheet boosted the conductivities of both Na^+ and electrons. These effects synergistically resulted in faster diffusion of Na^+ during uptake/removal and efficient transport of electrons of the P-$MoSe_2$/N-CNT NF. Additionally, the 1-D nanostructure is favorable for the electronic transmission of the kinetic processes and confinement effects of electronic structures derived from the nanoscale dimensions, which enable P-$MoSe_2$/N-CNT NF to interact more efficiently with Na^+, resulting in high-rate properties.

In order to understand the high-rate capability of P-$MoSe_2$/N-CNT NF in NIBs, the electrochemical kinetics of the cell are investigated via CV at various scan rates over the potential range of 0.001–3.0 V, as shown in Fig. 8a. The capacitive contribution can be analyzed by the relationships $i = av^b$ and $\log(i) = b\log(v) + \log(a)$, where i is the peak current, v is the scan rate, a is a constant, and b can vary from 0.5 to 1.0 [57,58]. When the b value is close to 1.0, the surface capacitive behavior

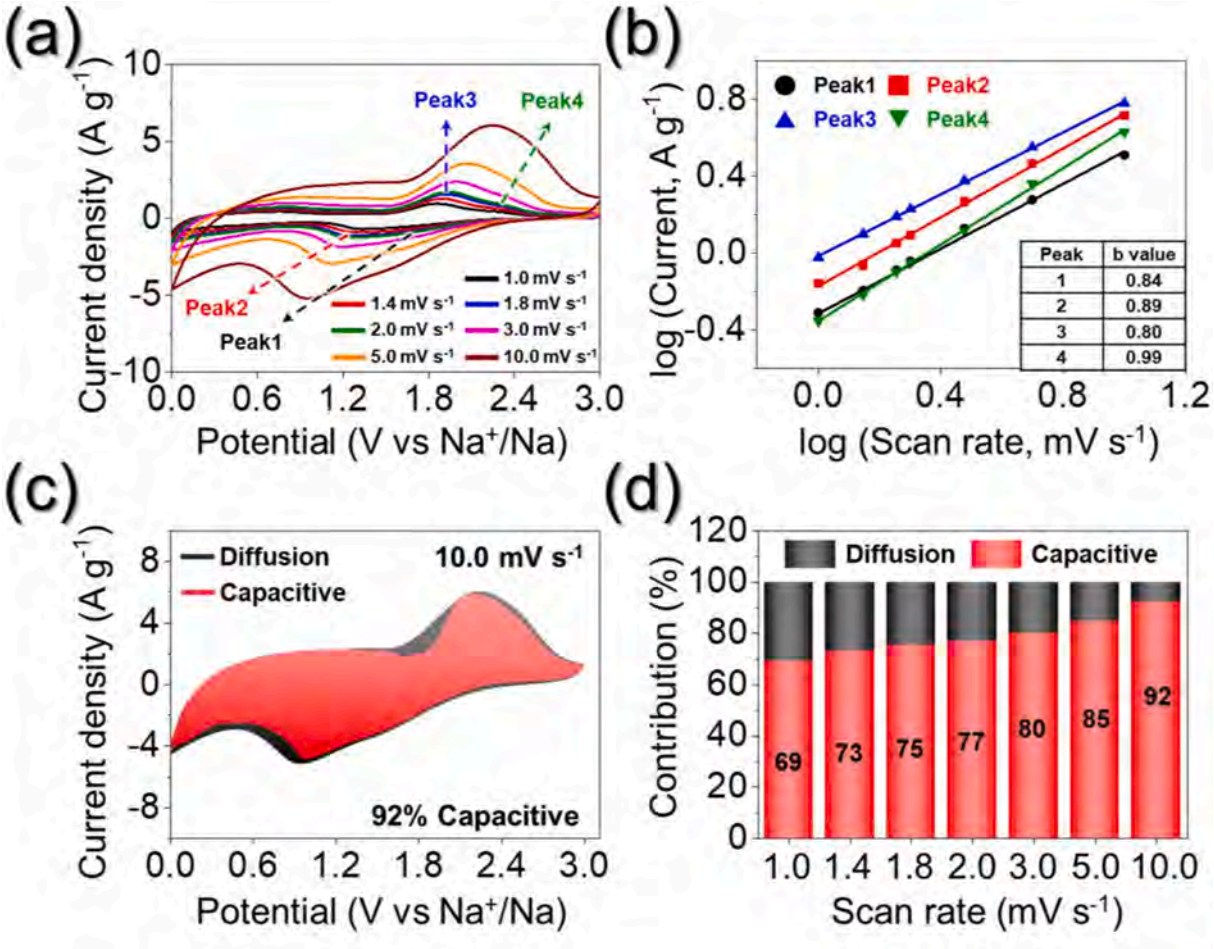

Fig. 8. Electrochemical reaction dynamics analysis of P-$MoSe_2$/N-CNT NF: (a) CV curves obtained at various scan rates, (b) current response *(i)* vs. scan rate *(n)* at each redox peak, (c) CV curve with the capacitive fraction shown by the red region at a scan rate of 10.0 mV s^{-1}, and (d) bar chart showing the percentage of the capacitive contribution at different scan rates.

dominates the reaction [59]. The *b* values for peaks 1, 2, 3, and 4 of P-$MoSe_2$/N-CNT NF are calculated to be 0.84, 0.89, 0.80, and 0.99, respectively, which are closer to 1.0 than are the *b* values of bare-$MoSe_2$ (0.74, 0.82, 0.75, and 0.85 for peaks 1, 2, 3, and 4, respectively), as shown in Fig. 8b and S11b. This suggested that the electrochemical reaction of P-$MoSe_2$/N-CNT NF is more driven by capacitive behavior compared to that in bare-$MoSe_2$. In general, the capacitive effect of electrode materials is closely related to the reaction kinetics; this means that as the contribution of the capacitive-controlled process increases, the transport kinetics will improve and, hence, the rate properties of the cells will be enhanced. Therefore, for quantitative analysis of the capacity contribution to the current response, the total charge stored in the electrode material was separated into capacitive-controlled and diffusion-limited processes, using the equation $i = k_1v + k_2v^{1/2}$, where k_1v and $k_2v^{1/2}$ represent the contributions from the capacitive effect and diffusion-controlled process, respectively [45,51]. At a scan rate of 10.0

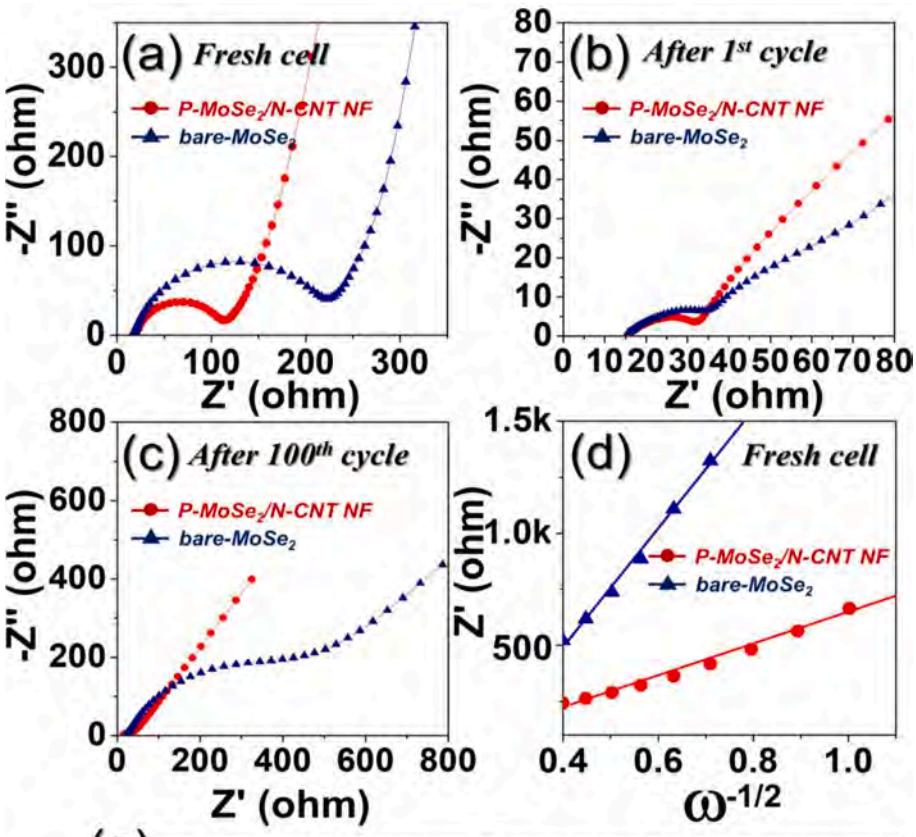

(e)

Sample	Cycles	R_e (Ω)	R_{ct} (Ω)	D_{Na^+} ($cm^2 \cdot s^{-1}$)
P-$MoSe_2$/N-CNT NF	fresh	17	95	1.1×10^{-12}
	1st	15	23	
	100th	15	21	
bare-$MoSe_2$	fresh	20	216	2.1×10^{-13}
	1st	20	36	
	100th	21	909	

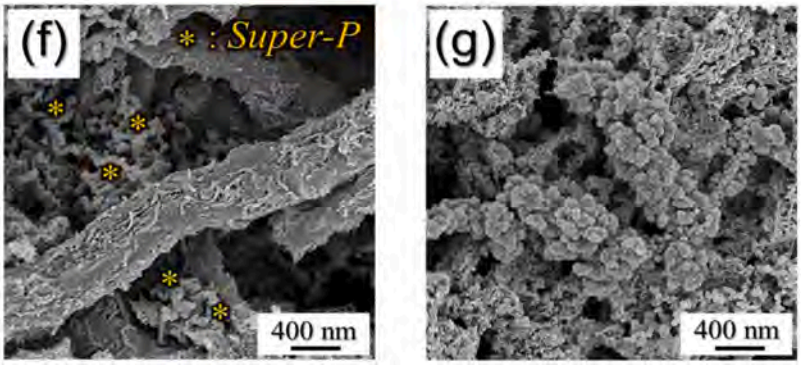

Fig. 9. (a–c) Nyquist impedance plots, (d) relationships between the real part of the impedance (Z_{re}) and $\omega^{-1/2}$, (e) typical parameters, and (f,g) FE-SEM images of P-$MoSe_2$/N-CNT NF and bare-$MoSe_2$ powders after 100 cycles at 0.2 A g^{-1}: (a) before cycling, (b) after the 1st cycle, (c) after the 100th cycle, (d) before cycling, (e) typical parameters, (f) P-$MoSe_2$/N-CNT NF, and (g) bare-$MoSe_2$ powders.

mV s^{-1}, as shown in Fig. 8c, the capacitive contribution of P-$MoSe_2$/N-CNT NF is calculated as 92%, which matches well with the high *b* values close to 1.0. On the contrary, bare-$MoSe_2$ has a lower percentage for the capacitive process, 75%, as shown in Fig. S11c. The capacitive contributions of P-$MoSe_2$/N-CNT NF at various scan rates are also calculated, as shown in Fig. 8d. The unique nanostructured P-$MoSe_2$/N-CNT NF delivers 69, 73, 75, 77, 80, 85, and 92% contributions from the capacitive effect at 1.0, 1.4, 1.8, 2.0, 3.0, 5.0, and 10.0 mV s^{-1}, respectively, which are larger than the capacitive contributions of bare-$MoSe_2$ (49, 52, 54, 55, 58, 64, and 75% at 1.0, 1.4, 1.8, 2.0, 3.0, 5.0, and 10.0 mV s^{-1}, respectively). The high ratio of the capacitive-controlled contribution of P-$MoSe_2$/N-CNT NF resulted in fast transport kinetics of Na^+, improving the rate capabilities of the electrodes. The synergetic effects of the N-CNT matrix, uniformly dispersed mesopores, and few-layered $MoSe_2$ nanosheets resulted in faster diffusion of Na^+ uptake/removal and efficient transport of electrons by improving the electrical contact between the active sites of the $MoSe_2$ nanosheets and the electrode.

EIS was also carried out to further prove the excellent Na^+ storage properties of the P-$MoSe_2$/N-CNT NF by investigating the kinetics of the samples. Nyquist plots of the samples before and after the 1st and 100th cycles are obtained via deconvolution using a Randle-type equivalent circuit model (Fig. S12). Based on previous reports [36,38], R_e represents the resistance of the electrolyte, R_{ct} represents the charge-transfer resistance of the electrode/electrolyte interface, while the low-frequency region corresponds to the diffusion of Na^+ within the electrodes [60–62]. In Fig. 9a, the P-$MoSe_2$/N-CNT NF has a lower R_{ct} value of 95 Ω compared to that of bare-$MoSe_2$ (216 Ω) before cycling. The $MoSe_2$ with few-layered nanosheets, pores, and N-CNTs could boost the conductivities of both Na^+ and electrons compared to larger and thicker stacked bare-$MoSe_2$ sheets by increasing the contact area between the electrolyte and $MoSe_2$ nanosheets, which lowers the charge transfer resistance of the P-$MoSe_2$/N-CNT NF. Moreover, R_e values are 17 Ω for P-$MoSe_2$/N-CNT NF and 20 Ω for the bare-$MoSe_2$, respectively. In Fig. 9b, the R_{ct} values of the two samples abruptly decrease to 23 Ω for the P-$MoSe_2$/N-CNT NF and 36 Ω for bare-$MoSe_2$, after the 1st cycle. This is due to the transformation of the $MoSe_2$ nanosheets into ultrafine nanocrystals during the initial cycling [8]. After the 100th cycle, the R_{ct} values of P-$MoSe_2$/N-CNT NF and bare-$MoSe_2$ are 21 and 909 Ω, respectively. The high structural stability of P-$MoSe_2$/N-CNT NF could accommodate the volume changes of the $MoSe_2$ nanosheets during repeated sodiation/desodiation cycles. However, the structure of bare-$MoSe_2$ disintegrated over 100 cycles, resulting in a much higher R_{ct} value. Fig. 9d shows the relationship between Z_{re} and $\omega^{-1/2}$ in the low-frequency region. The lower gradient in the low-frequency region of the P-$MoSe_2$/N-CNT NF plot indicates that the Na^+ diffusivity in the structure is higher than that of bare-$MoSe_2$. The thin and few-layered $MoSe_2$ sheets, numerous uniformly dispersed mesopores, and N-CNT matrix could be responsible for the higher Na^+ diffusivity of the P-$MoSe_2$/N-CNT NF. The Na^+ ion diffusion coefficient (D_{Na+}) values of the samples were calculated using the following equation [14,58,63]:

$$DNa^+ = 0.5R^2T^2/A^2F^4C^2\sigma_W^2 \quad (1)$$

In Equation (1), *R* is the gas constant, *T* is the temperature, *A* is the electrode area, *C* is the Na^+ concentration, *F* is the Faraday constant, and σ_W is the Warburg impedance factor. The D_{Na+} values for P-$MoSe_2$/N-CNT NF and bare-$MoSe_2$ are 1.1×10^{-12} and 2.1×10^{-13} cm^2 s^{-1}, respectively. The approximately five-fold higher D_{Na+} value of P-$MoSe_2$/N-CNT NF suggests better Na^+ diffusion and, therefore, enhanced redox reaction kinetics. To evaluate the structural stability, the morphology of the P-$MoSe_2$/N-CNT NF after 100 cycles is inspected, as shown in Fig. 9f. Impressively, the P-$MoSe_2$/N-CNT NF maintains their original 1-D CNT matrixed nanostructure well even after long cycling. In Fig. S13, EDS mapping images of the cycled P-$MoSe_2$/N-CNT NF further confirm the well-preserved structure along with the uniform distribution of Mo, Se, C, and N contents of the composite with Na originating from the electrolyte decomposition. However, the structure of bare-$MoSe_2$ is completely destroyed and subsequently agglomerates after cycling, as shown in Fig. 9g. The results prove a robust structure of P-$MoSe_2$/N-CNT NF, ensuring good tolerance of the composite against the huge volume expansion during repeated Na^+ insertion and desertion.

4. Conclusions

In this study, N-CNTs were highly densified and entangled in nanofiber structure along with few-layered $MoSe_2$ nanosheets for use as anodes in NIBs by electrospinning and a two-step heat treatment. To maximize the electrical conductivity of the composite, the amorphous carbon formed by PAN decomposition was selectively removed as a gas except N-CNTs by an intermediate heat treatment. During this step, numerous mesopores were also formed between the N-CNTs and MoO_3 crystals. Simple selenization finally resulted in the formation of N-CNT matrixed porous nanofibers decorated with few-layered $MoSe_2$ nanosheets. The N-CNTs significantly improved the overall electrical conductivity of the $MoSe_2$ composite, and the uniformly dispersed pores enabled efficient penetration of the liquid electrolyte into the structure during cycling. Moreover, the few-layered $MoSe_2$ nanosheets boosted the conductivities of Na^+ and electrons. Thus, these synergistically resulted in the faster diffusion of Na^+ during uptake/removal and efficient transport of electrons of the P-$MoSe_2$/N-CNT NF when used as anodes for NIBs. The 1-D nanostructure was also favorable for the electronic transmission of the kinetic processes and confinement effects of electronic structures derived from the nanoscale dimensions, which enabled the P-$MoSe_2$/N-CNT NF to interact more efficiently with Na^+, resulting in high Na^+ storage properties. Consequently, the proposed strategy to synthesize unique P-$MoSe_2$/N-CNT NF structures in this study can be applicable to other materials for energy storage fields.

Declaration of Competing Interest

The authors declare that they have no known competing financial interests or personal relationships that could have appeared to influence the work reported in this paper.

Acknowledgements

This work was supported by the National Research Foundation of Korea (NRF) grant funded by the Korean government (MSIP) (NRF-2021R1A4A200168711, NRF-2017M1A2A2087577, NRF-2018R1D1A3B07042514).

Appendix A. Supplementary data

Supplementary data to this article can be found online at https://doi.org/10.1016/j.cej.2021.129051.

References

[1] S. Chen, C. Wu, L. Shen, C. Zhu, Y. Huang, K. Xi, J. Maier, Y. Yu, Adv. Mater. 29 (2017) 1700431.
[2] Y. Chen, X. Yuan, C. Yang, Y. Lian, A.A. Razzaq, R. Shah, J. Guo, X. Zhao, Y. Peng, J. Alloy. Compd. 777 (2019) 127–134.
[3] Y. Dou, Y. Wang, D. Tian, J. Xu, Z. Zhang, Q. Liu, B. Ruan, J. Ma, Z. Sun, S.X. Dou, 2D Mater. 4 (2016), 015022.
[4] J.S. Cho, S.Y. Lee, Y.C. Kang, Sci. Rep. 6 (2016) 1–10.
[5] Y. Liu, Y. Xu, Y. Han, Z. Zhang, J. Xu, Y. Du, J. Bao, X. Zhou, J. Power Sources 436 (2019), 226860.
[6] M.S. Jo, J.S. Lee, S.Y. Jeong, J.K. Kim, Y.C. Kang, D.W. Kang, S.M. Jeong, J.S. Cho, Small 16 (2020) 2003391.
[7] Z. Zhang, X. Shi, X. Yang, Y. Fu, K. Zhang, Y. Lai, J. Li, A.C.S. Appl, Mater. Interfaces 8 (2016) 13849–13856.
[8] W. Kang, Y. Wang, D. Cao, Z. Kang, D. Sun, J. Alloy. Compd. 743 (2018) 410–418.
[9] J.K. Kim, S.Y. Jeong, S.H. Lim, J.H. Oh, S.K. Park, J.S. Cho, Y.C. Kang, Chem. Asian J. 14 (2019) 3127–3140.
[10] G. Lindberg, A. Larsson, M. Råberg, D. Boström, R. Backman, A. Nordin, J. Chem. Thermodyn. 39 (2007) 44–48.

[11] M. Chhowalla, H.S. Shin, G. Eda, L.-J. Li, K.P. Loh, H. Zhang, Nat. Chem. 5 (2013) 263–275.
[12] Y. Tang, Z. Zhao, Y. Wang, Y. Dong, Y. Liu, X. Wang, J. Qiu, A.C.S. Appl, Mater. Interfaces 8 (2016) 32324–32332.
[13] F. Niu, J. Yang, N. Wang, D. Zhang, W. Fan, J. Yang, Y. Qian, Adv. Funct. Mater. 27 (2017) 1700522.
[14] M. Yousaf, Y. Wang, Y. Chen, Z. Wang, A. Firdous, Z. Ali, N. Mahmood, R. Zou, S. Guo, R.P. Han, Energy Mater. 9 (2019) 1900567.
[15] X. Zhao, W. Cai, Y. Yang, X. Song, Z. Neale, H.-E. Wang, J. Sui, G. Cao, Nano Energy 47 (2018) 224–234.
[16] S.-K. Park, Y.C. Kang, A.C.S. Appl, Mater. Interfaces 10 (2018) 17203–17213.
[17] J. Li, D. Yan, S. Hou, T. Lu, Y. Yao, L. Pan, Chem. Eng. J. 354 (2018) 172–181.
[18] W. Ren, H. Zhang, C. Guan, C. Cheng, Adv. Funct. Mater. 27 (2017) 1702116.
[19] J.S. Cho, J.-S. Park, Y.C. Kang, Nano Res. 10 (2017) 897–907.
[20] Y. Liu, N. Zhang, L. Jiao, J. Chen, Adv. Mater. 27 (2015) 6702–6707.
[21] S.H. Oh, O.H. Kwon, Y.C. Kang, J.-K. Kim, J.S. Cho, J. Mater. Chem. A 7 (2019) 12480–12488.
[22] N. Sun, C.-L. Peng, J.-C. Zheng, Z.-J. He, H. Tong, L.-B. Tang, C.-S. An, B. Xiao, Powder Technol. 338 (2018) 211–219.
[23] B. Wang, H. Xin, X. Li, J. Cheng, G. Yang, F. Nie, Sci. Rep. 4 (2014) 3729.
[24] N.T.H. Trang, Z. Ali, D.J. Kang, A.C.S. Appl, Mater. Interfaces 7 (2015) 3676–3683.
[25] Z. Aly, A. Graulet, N. Scales, T. Hanley, Sci. Pollut. Res. 21 (2014) 3972–3986.
[26] S.-B. Yoon, E.-H. Yoon, K.-B. Kim, J. Power Sources 196 (2011) 10791–10797.
[27] R. Iwamoto, K. Oguro, M. Sato, Y. Iseki, J. Phys. Chem. B 106 (2002) 6973–6979.
[28] M. Raja, S.H. Ryu, A. Shanmugharaj, Eur. Polym. J. 49 (2013) 3492–3500.
[29] S.Y. Jeong, S.-K. Park, Y.C. Kang, J.S. Cho, Chem. Eng. J. 351 (2018) 559–568.
[30] P. Ge, H. Hou, C.E. Banks, C.W. Foster, S. Li, Y. Zhang, J. He, C. Zhang, X. Ji, Energy Stor. Mater. 12 (2018) 310–323.
[31] B. Li, Y. Liu, Y. Li, S. Jiao, S. Zeng, L. Shi, G. Zhang, A.C.S. Appl, Mater. Interfaces (2019) 2390–2399.
[32] G. Jia, H. Wang, D. Chao, H. He, N.H. Tiep, Y. Zhang, Z. Zhang, H.J. Fan, Nanotechnology 28 (2017) 42LT01.
[33] Z. Zhang, S. Ye, J. Ji, Z. Li, F. Wang, Colloids Surf. A Physicochem. Eng. Asp. (2020), 124888.
[34] D. Zheng, P. Cheng, Q. Yao, Y. Fang, M. Yang, L. Zhu, L. Zhang, J. Alloys Compd. 848 (2020), 156588.
[35] H. Liu, B. Liu, H. Guo, M. Liang, Y. Zhang, T. Borjigin, X. Yang, L. Wang, X. Sun, Nano Energy 51 (2018) 639–648.
[36] J.S. Cho, J.-S. Park, K.M. Jeon, Y.C. Kang, J. Mater. Chem. A 5 (2017) 10632–10639.
[37] T. Xiang, S. Tao, W. Xu, Q. Fang, C. Wu, D. Liu, Y. Zhou, A. Khalil, Z. Muhammad, W. Chu, ACS Nano 11 (2017) 6483–6491.
[38] J.S. Cho, J.M. Won, J.-K. Lee, Y.C. Kang, Nano Energy 26 (2016) 466–478.
[39] J. Zhou, J. Yang, Z. Xu, T. Zhang, Z. Chen, J. Wang, J. Mater. Chem. A 5 (2017) 9350–9357.
[40] W.-G. Lim, C. Jo, J. Lee, D.S. Hwang, Korean J. Chem. Eng. 35 (2018) 579–586.
[41] S.-K. Park, A. Jin, S.-H. Yu, J. Ha, B. Jang, S. Bong, S. Woo, Y.-E. Sung, Y. Piao, Electrochim. Acta 120 (2014) 452–459.
[42] Q. Guo, Y. Ma, T. Chen, Q. Xia, M. Yang, H. Xia, Y. Yu, ACS Nano 11 (2017) 12658–12667.
[43] Y.-C. Zhang, Y. You, S. Xin, Y.-X. Yin, J. Zhang, P. Wang, X.-S. Zheng, F.-F. Cao, Y.-G. Guo, Nano Energy 25 (2016) 120–127.
[44] Y. Huang, H. Lu, H. Gu, J. Fu, S. Mo, C. Wei, Y.-E. Miao, T. Liu, Nanoscale 7 (2015) 18595–18602.
[45] J. Yang, J. Zhu, J. Xu, C. Zhang, T. Liu, A.C.S. Appl, Mater. Interfaces 9 (2017) 44550–44559.
[46] W. Zhao, X. Ma, ACS Sustain, Chem, Eng, 2020.
[47] L. Zeng, B. Kang, F. Luo, Y. Fang, C. Zheng, J. Liu, R. Liu, X. Li, Q. Chen, M. Wei, Chem. Eur. J. 25 (2019) 13411–13421.
[48] F. Zheng, W. Zhong, Q. Deng, Q. Pan, X. Ou, Y. Liu, X. Xiong, C. Yang, Y. Chen, M. Liu, Chem. Eng. J. 357 (2019) 226–236.
[49] Q. Su, X. Cao, T. Yu, X. Kong, Y. Wang, J. Chen, J. Lin, X. Xie, S. Liang, A. Pan, J. Mater. Chem. A 7 (2019) 22871–22878.
[50] Z.T. Shi, W. Kang, J. Xu, L.L. Sun, C. Wu, L. Wang, Y.Q. Yu, D.Y. Yu, W. Zhang, C. S. Lee, Small 11 (2015) 5667–5674.
[51] P. Ge, L. Zhang, Y. Yang, W. Sun, Y. Hu, X. Ji, Adv. Mater. Interfaces 7 (2020) 1901651.
[52] J.S. Lee, M.S. Jo, R. Saroha, D.S. Jung, Y.H. Seon, J.S. Lee, Y.C. Kang, D.W. Kang, J. S. Cho, Small 16 (2020) 2002213.
[53] H. Ma, S. Du, H. Tao, T. Li, Y. Zhang, J. Electroanal. Chem. 823 (2018) 307–314.
[54] J.-S. Do, C.-H. Weng, J. Power Sources 146 (2005) 482–486.
[55] Z.-S. Wu, W. Ren, L. Wen, L. Gao, J. Zhao, Z. Chen, G. Zhou, F. Li, H.-M. Cheng, ACS Nano 4 (2010) 3187–3194.
[56] G. Zhou, D.-W. Wang, F. Li, L. Zhang, N. Li, Z.-S. Wu, L. Wen, G.Q. Lu, H.-M. Cheng, Chem. Mater. 22 (2010) 5306–5313.
[57] H. Kim, K. Lim, G. Yoon, J.H. Park, K. Ku, H.D. Lim, Y.E. Sung, K. Kang, Energy Mater. 7 (2017) 1700418.
[58] L.-B. Tang, B. Zhang, C.-S. An, H. Li, B. Xiao, J.-H. Li, Z.-J. He, J.-C. Zheng, Inorg. Chem. 58 (2019) 8169–8178.
[59] Y.-Y. Wang, H. Fan, B.-H. Hou, X.-H. Rui, Q.-L. Ning, Z. Cui, J.-Z. Guo, Y. Yang, X.-L. Wu, J. Mater. Chem. A 6 (2018) 22966–22975.
[60] A.K. Haridas, J. Heo, X. Li, H.-J. Ahn, X. Zhao, Z. Deng, M. Agostini, A. Matic, J.-H. Ahn, Chem. Eng. J. 385 (2020), 123453.
[61] J.-Y. Kim, K.-Y. Shin, M.H. Raza, N. Pinna, Y.-E. Sung, Korean J. Chem. Eng. 36 (2019) 1157–1163.
[62] H. Lee, C. Han, T. Park, Korean J. Chem. Eng. 37 (2020) 577–582.
[63] Y. Cao, Y. Liu, D. Zhao, J. Zhang, X. Xia, T. Chen, L.-C. Zhang, P. Qin, Y. Xia, J. Alloy. Compd. 784 (2019) 939–946.